Piggybacking functionalized DNA nanostructures into live-cell nuclei

Golbarg Roozbahani, P. Colosi, Attila Oravecz, Elena Sorokina, Wolfgang Pfeifer, Siamak Shokri, Yin Wei, Pascal Didier, Marcello Deluca, Gaurav Arya, et al.

SYNTHETIC BIOLOGY

Piggybacking functionalized DNA nanostructures into live-cell nuclei

Golbarg M. Roozbahani[1,2]†, P. L. Colosi[3]†, Attila Oravecz[4,5,6,7]†, Elena M. Sorokina[3], Wolfgang Pfeifer[1,2], Siamak Shokri[1], Yin Wei[8], Pascal Didier[7,9], Marcello DeLuca[10], Gaurav Arya[10], László Tora[4,5,6,7]*, Melike Lakadamyali[3,11,12]*, Michael G. Poirier[1,8,13]*, Carlos E. Castro[2,8]*

DNA origami nanostructures (DOs) are promising tools for applications including drug delivery, biosensing, detecting biomolecules, and probing chromatin substructures. Targeting these nanodevices to mammalian cell nuclei could provide impactful approaches for probing, visualizing, and controlling biomolecular processes within live cells. We present an approach to deliver DOs into live-cell nuclei. We show that these DOs do not undergo detectable structural degradation in cell culture media or cell extracts for 24 hours. To deliver DOs into the nuclei of human U2OS cells, we conjugated 30-nanometer DO nanorods with an antibody raised against a nuclear factor, specifically the largest subunit of RNA polymerase II (Pol II). We find that DOs remain structurally intact in cells for 24 hours, including inside the nucleus. We demonstrate that electroporated anti–Pol II antibody–conjugated DOs are piggybacked into nuclei and exhibit subdiffusive motion inside the nucleus. Our results establish interfacing DOs with a nuclear factor as an effective method to deliver nanodevices into live-cell nuclei.

INTRODUCTION

Recent advances in DNA nanotechnology have presented promising opportunities for applications in areas like drug delivery, biosensing, and biomanufacturing (*1*–*3*). In particular, DNA origami (DO) (*4*), where a long template strand is folded into a compact shape by base-pairing with many shorter strands, enables fabrication of nanostructures with complex and precise shape, custom functionalization, and tunable mechanical properties (*5*, *6*). These features make DO devices attractive as platforms for targeted therapies (*7*), biophysical measurements (*8*), or controlling molecular interactions (*9*, *10*). Many of these applications either require or can be enhanced by effective methods to deliver DOs into intracellular environments. Prior studies have demonstrated uptake of DO into cells (*11*–*13*), but the trafficking of DOs upon entry into live cells and specifically to nuclei is less well understood and/or developed. Methods for the efficient targeting of DOs into live-cell nuclei could greatly enhance existing applications in therapeutic delivery, for example, gene delivery (*14*–*16*), and could enable translation of other functions of DO like biophysical measurement or imaging into cell nuclei.

The nucleus houses the cell's genetic material and the machinery essential for transcription and other processes vital to gene expression and regulation (*17*, *18*). Consequently, targeting molecular structures and devices to the nucleus is an attractive approach for many therapies and may present opportunities for nanoscale tools to probe or control the genetic or epigenetic processes that regulate cell function. For example, recent in vitro work has demonstrated nanodevices as tools for sequestering or organizing biomolecules or larger complexes (*19*–*21*), imaging biomolecules at high resolution (*22*, *23*), and manipulating enzymatic reactions (*24*, *25*), all of which could be useful inside cells and cellular compartments. Delivering DO nanodevices to cell nuclei is attractive for applications like nucleic acid detection (*26*, *27*), biophysical probing of chromatin substructures [previously demonstrated in vitro (*28*, *29*)], and gene delivery (*14*–*16*).

While several efforts have studied the delivery and uptake of DO nanostructures into live cells (*11*, *13*, *30*, *31*), only recently has the specific delivery of DO structures to the nucleus been explored, focused in the context of gene delivery (*14*–*16*, *32*). These studies have established DOs as useful tools for the delivery of genetic information into live cells. Although these prior studies focused on gene expression, key questions remain unclear: (i) Are these DO structures stable inside the cell? (ii) How many of the DO structures reach the nuclei? (iii) Can intact DOs be delivered into the nucleus? Hence, there remains a critical need for robust methods to deliver DO nanostructures to live-cell nuclei, which would be an essential step to enabling intranuclear functions that rely on the structure and not just the encoded sequence.

Here, we present a novel approach for the delivery of intact DO nanostructures into live cells and specifically to the nucleus (Fig. 1). Inspired by recent work focused on the delivery of antibodies into live-cell nuclei (*33*–*35*), our method involves the conjugation of DO nanostructures to antibodies that bind to neosynthetized proteins in the cytoplasm, which function in the nucleus and thus naturally cycle to the nucleus, thereby carrying or "piggybacking," the DOs along with them. We chose the large subunit of RNA polymerase Pol II, a pivotal enzyme involved in gene transcription, as a molecule to target the neosynthetized subunit in the cytoplasm. Our prior work demonstrated that the piggybacking approach is effective for the delivery

[1]Department of Physics, The Ohio State University, Columbus, OH 43210, USA. [2]Department of Mechanical and Aerospace Engineering, The Ohio State University, Columbus, OH 43210, USA. [3]Department of Physiology, University of Pennsylvania, Philadelphia, PA 19104, USA. [4]Institut de Génétique et de Biologie Moléculaire et Cellulaire, Illkirch 67404, France. [5]Centre National de la Recherche Scientifique, UMR7104, Illkirch 67404, France. [6]Institut National de la Santé et de la Recherche Médicale, U1258, Illkirch 67404, France. [7]Université de Strasbourg, Illkirch 67404, France. [8]Biophysics Graduate Program, The Ohio State University, Columbus, OH 43210, USA. [9]Laboratoire de Biophotonique et Pharmacologie, Illkirch 67401, France. [10]Department of Mechanical Engineering and Materials Science, Duke University, Durham, NC 27708, USA. [11]Department of Cell and Developmental Biology, University of Pennsylvania, Philadelphia, PA 19104, USA. [12]Epigenetics Institute, University of Pennsylvania, Philadelphia, PA 19104, USA. [13]Department of Chemistry and Biochemistry, The Ohio State University, Columbus, OH 43210, USA.
*Corresponding author. Email: laszlo@igbmc.fr (L.T.); melikel@pennmedicine.upenn.edu (M.L.); poirier.18@osu.edu (M.G.P.); castro.39@osu.edu (C.E.C.)
†These authors contributed equally to this work.

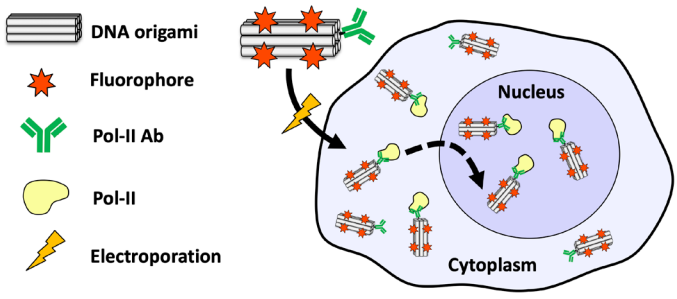

Fig. 1. Concept for piggybacking DO nanostructures into the nucleus. DO nanostructures functionalized with RNA Pol II–targeting antibodies and eight Cy5 fluorophores are electroporated into cells, bound to Pol II, and then are imported, or piggybacked, into the nucleus.

of antibodies with high affinity toward Pol II into live-cell nuclei (*33*). Here, we show that, after electroporation into the cytoplasm, Pol II antibody–conjugated 30-nm nanorod DO structures can enter the nuclei of U2OS cells, as confirmed by fluorescence microscopy, and exhibit subdiffusive motion within live-cell nuclei. We also studied the stability of DO in cell culture media and different cell lysates using gel electrophoresis and transmission electron microscopy (TEM) and inside live cells using fluorescence imaging. These analyses reveal the structural integrity of the DO over extended periods in cell media and extracts and confirm that DOs remain structurally stable 24 hours after electroporation both in the cytoplasm and after piggybacking into the nucleus. Combined, our results establish a basis to implement DO nanodevices as tools for imaging, detection, biophysical measurements, or other applications inside cell nuclei.

RESULTS

Design and fabrication of DO nanostructures

To develop DO devices that are effective in cellular environment, we prioritized designs similar to structures previously shown to be stable in physiological conditions and resistant to degradation (*36*, *37*). We therefore focused on two rod structures with square lattice cross sections. The eight-helix bundle (8HB) was designed in caDNAno (*38*), and the 26HB design has been previously reported (*36*, *37*, *39*). Both the 8HB (~6 nm by 6 nm cross section and length of ~30 nm, molecular weight of ~0.5 MDa) and the 26HB origami structures (~10 nm by 12 nm cross section with a length of ~90 nm, molecular weight of ~4.8 MDa) were evaluated using coarse-grained molecular dynamics (MD) simulations with the oxDNA model (*40*, *41*) confirming a well-defined nanorod shape (Fig. 2A and fig. S1). The DO structures were fabricated via molecular self-assembly and evaluated by gel electrophoresis and TEM (Fig. 2, A and B, and figs. S1 and S2). We leveraged the specific labeling capabilities of DO by adding single-stranded DNA (ssDNA) overhangs protruding from the structure to bind complementary strands with desired functionalities. The design included eight side overhangs, specifically tailored for fluorophore labeling by binding to a complementary oligonucleotide labeled with a fluorescent Cy3 or Cy5 molecule. Overhangs for Cy3 and for Cy5 had distinct sequences to allow for attaching a defined number of each. In addition, one or two ssDNA overhangs were included on one end of the DO to facilitate antibody attachment.

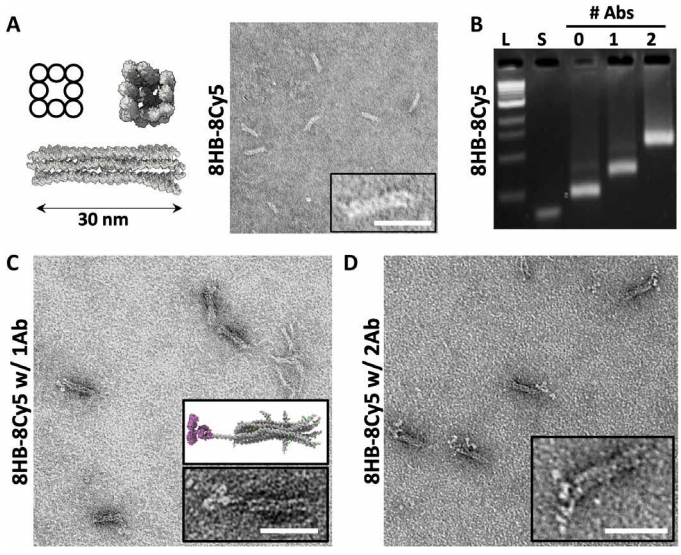

Fig. 2. Fabrication and antibody labeling of DO nanostructures. (**A**) Design schematic, oxDNA simulation, and TEM image of the 8HB DO structure. The simulation model depicts the base structure without the eight overhangs for fluorophore attachment. (**B**) Gel electrophoresis illustrates clear and efficient labeling of DO with one or two RNA Pol II antibodies (Abs) indicated by mobility shifts. TEM imaging confirmed efficient functionalization with one (**C**) or two (**D**) antibodies. Insets show a zoomed-in depiction of a single functionalized DO structure [compared to simulated 8HB structure with overhangs for fluorophore labels and antibody attached for size reference in (C)]. Scale bars, 30 nm.

After the addition of fluorophore-labeled strands and purification, the functionalized DO nanostructures were characterized by gel electrophoresis and TEM imaging (8HB shown in Fig. 2, and 26HB shown in fig. S1). Since the 26HB design was previously reported and characterized (*36*, *37*), here, we focused our analysis on the 8HB. Gel electrophoresis revealed well-folded populations of 8HB structures with a single dominant population after purification by electroelution. Structures labeled with antibodies exhibited decreased mobility with clear shifts between DO with 0, 1, and 2 antibodies with labeling yields of ~70% or better (fig. S2) with electroelution purification effectively removing unlabeled DO (Fig. 2B). TEM imaging revealed well-folded nanorod-shaped structures about 30 nm in length, and one or two antibodies were visible for the single or double antibody–labeled designs (Fig. 2, C and D, and fig. S3). The insets in Fig. 2 (C and D) show zoomed-in TEM images of the labeled 8HB, and, for the single antibody label, a simulated version is also shown for comparison. We only studied the effects of antibody number on the 8HB, so the 26HB was only labeled with a single antibody (fig. S1). These findings highlight the precision of the design and emphasize the controlled assembly and specific labeling capabilities of the structure.

Stability of DO nanostructures in biological solutions

To confirm the suitability of the fabricated DO structures for intracellular applications, we first tested the stability of the structures in multiple relevant biological solutions including cell culture media and cellular cytoplasmic and nuclear extracts prepared from human cells (U2OS). We monitored the structural integrity of DO over a 24-hour period using agarose gel electrophoresis, imaging gels in

the Cy5 channel to confirm stability of overhang attachment. Hereafter, we refer to the DO with fluorophores added to the eight attachment sites as 8HB-8Cy5 or 26HB-8Cy5. Gel analysis revealed that structures consistently showed the same gel mobility and intensity, indicating structural integrity and stability in cell media (8HB-8Cy5 results in Fig. 3A and fig. S4, and 26HB-8Cy5 results in fig. S5), which is consistent with prior studies on the 26HB design (*37*). This analysis was extended to extracts to consider the stability inside cells, revealing that the 8HB-8Cy5 and 26HB-8Cy5 remained highly stable throughout the 24-hour monitoring period in U2OS cytoplasmic and nuclear extracts (8HB-8Cy5 results in Fig. 3, B and C and fig. S6, and 26HB-8Cy5 results in fig. S7). For TEM imaging, we focused on the 24-hour time point in the nuclear extract as the most relevant condition. TEM analysis further demonstrated intact structures in nuclear extract at the 24-hour time point (Fig. 3C and figs. S6 and S7). While it is challenging to accurately recapitulate an intracellular environment, these results suggest that these DOs can remain stable over extended times in the presence of cytoplasmic and nuclear components. Hence, these results indicate that DO nanostructures could be well suited for intracellular applications that require the structure to remain intact, although the integrity of the structure once introduced directly inside live cells is still important to verify, which we address subsequently.

Electroporation of DO structures into U2OS cells

We chose electroporation as a mechanism to get DO structures into cells, which has previously been demonstrated as an effective mechanism to deliver gene encoding DOs into live cells (*14*, *15*, *32*). To test the viability of electroporation for the delivery of intact DO into nuclei, we first performed electroporation experiments with 8HB-8Cy5 and 26HB-8Cy5 DO with no antibodies attached. These initial electroporation tests revealed that the 26HB exhibited significant aggregation when introduced into U2OS cells (fig. S8). We attribute this to the size of the 26HB (approximately 4.8 MDa or 7300 base pairs in total size); prior studies have shown similar aggregation behavior of other electroporated nanomaterials such as quantum dots (*42*), silver nanoparticles (*43*), and DNA plasmids (*44*). On the other hand, the 8HB exhibited minimal aggregation and distributed more homogeneously throughout the cell cytoplasm (fig. S8). Hence, we focused our experiments on the 8HB.

We also tested the efficacy of electroporation to deliver DOs to cells and the effect of electroporation on cell viability. Cells were

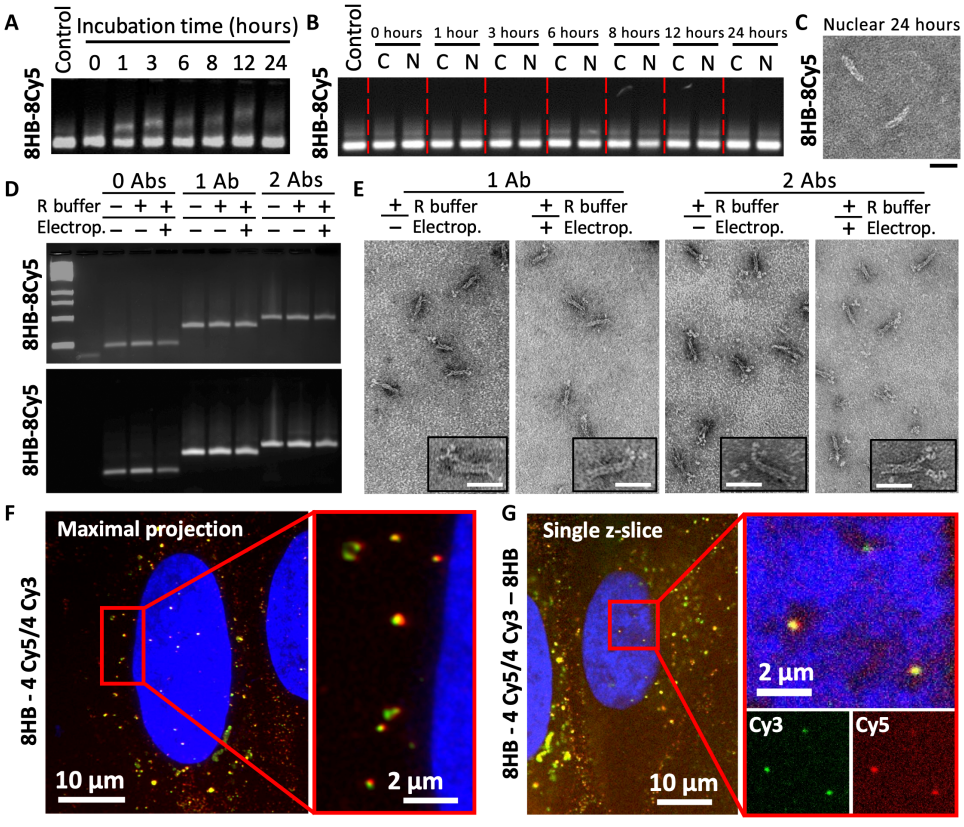

Fig. 3. Stability of DO nanostructures. (**A** and **B**) Agarose gel electrophoresis (images show Cy5 fluorophore emission) revealed consistent mobility when 8HB structures were incubated at 37°C in (A) cell culture media or (B) cytoplasmic (C) or nuclear (N) extract from U2OS cells, verifying structural stability and fluorophore attachment integrity up to 24 hours. (**C**) TEM imaging also confirmed that structures remain intact, shown for the 24-hour nuclear extract condition (Scale bar, 30 nm). (**D**) Agarose gel electrophoresis also revealed no changes in mobility in electroporation buffer (R buffer) and after being subjected to electroporation for structures alone or for structures with one or two antibodies (Ab) attached. The ethidium bromide stain is shown on top, and Cy5 emission channel at the bottom. (**E**) TEM imaging also confirmed that structures remain intact and antibodies remain attached in R buffer and after electroporation. Insets show zoomed-in views of a single 8HB structure with one or two antibodies attached (Scale bars, 30 nm). (**F** and **G**) 8HB double-labeled with Cy3 and Cy5 electroporated into U2OS cells exhibit colocalization of both fluorophores in the cytoplasm (F) and the nucleus (G). Scale bars are indicated in the panels and insets.

electroporated with either 8HB-8Cy5 structures or buffer as a control. The cells were then 4′,6-diamidino-2-phenylindole (DAPI)–stained 24 hours after electroporation and analyzed by flow cytometry (fig. S9). Viability was evaluated by exclusion of the DAPI-positive events, which revealed that 89.5 ± 0.7% (mean ± SD) of the control cells survived the electroporation procedure, while DO-electroporated cells showed only a subtle decrease of viability with 84 ± 4% survival rate on average (fig. S9A). Ninety-four ± five % of these live DO-electroporated cells were Cy5 positive on average, indicating that almost all the surviving cells harbored the Cy5-labeled DO structures (fig. S9, B and C).

Stability of DO nanostructures after electroporation

We next performed experiments to assess the stability of antibody-labeled 8HB before and after electroporation using gel electrophoresis and TEM. These experiments were carried out with DO labeled with anti–Pol II antibodies. As a control, we also tested the stability of DO in the manufacturer-provided R buffer used for cell resuspension before electroporation. Gel electrophoresis revealed that the structures (unlabeled and labeled with one or two anti–Pol II antibodies) exhibited similar mobility in R buffer before and after electroporation compared to a control structure kept in storage buffer and not subjected to electroporation (Fig. 3D). Gels were imaged both in the Cy5 channel and with ethidium bromide staining of the DNA, suggesting that the DO structure and the fluorophore and antibody labeling all remained intact after electroporation. TEM imaging of gel-purified samples confirmed that DO structures maintained their shape and antibody labeling in R buffer and after electroporation (Fig. 3E).

Stability of DO nanostructures in U2OS cells

To directly assess the stability of fluorophore-labeled nanostructures after transfection into cells, we performed electroporation experiments with DO labeled with two distinct color fluorophores Cy3 and Cy5 (i.e., double-labeled structures). We reasoned that if DO structures remain intact, the Cy3 and Cy5 emission would remain colocalized. Prior work has shown that even degradation products of DNA structures can exhibit fluorescence colocalization in cells (*45*). In addition, aggregation of DO structures can also lead to the appearance of colocalization. To account for these possibilities, we performed experiments in which 8HB structures were either double labeled with Cy3 and Cy5, or singly labeled with either Cy3 or Cy5, but coelectroporated into cells. If the 8HB structures and fluorophore labeling are stable, we predicted that the colocalization between Cy3 and Cy5 signal in double-labeled 8HB structures would be higher than in the co-electroporation with the single-color structures. On the other hand, if the 8HB structures were unstable (i.e., subject to intracellular degradation) or aggregated, we expected colocalization values similar to the cotransfection condition.

U2OS cells were electroporated with 8HB structures in both experimental configurations: 8HB structures double labeled with Cy3 and Cy5 and a cotransfection of 8HB labeled with Cy3 and 8HB labeled with Cy5. U2OS cells were fixed and nuclei stained 24 hours after electroporation. Cells were imaged with highly inclined and laminated optical sheet (HILO) illumination, and the nuclear stain was used to set the focus to the mid-plane of the nucleus. In addition, we carried out iSIM (instant structured illumination microscopy) imaging in which z-stacks were recorded throughout the volume of the nucleus. We observed clear visual colocalization of Cy3 and Cy5 signals in the double-labeled condition in both HILO and iSIM images, while cotransfection gave rise to visually lower levels of colocalization visualized via HILO imaging (Fig. 3, F and G, and fig. S10). To quantify the spatial correlation between the two signals, we calculated the average Pearson correlation coefficient, r, for the detected Cy3 and Cy5 fluorescence peaks in HILO images. The 8HB structures exhibited correlation coefficients of $r = 0.82 \pm 0.10$ for the double-labeled 8HB (8HB-4Cy5/4Cy3) and $r = 0.34 \pm 0.14$ for the cotransfected singly labeled 8HB (8HB-8Cy5 plus 8HB-8Cy3). These results suggest that the 8HB DO remain primarily intact inside cells up to 24 hours after electroporation. In the iSIM images, we observed 8HB DO inside the nucleus that exhibited colocalization, indicating that DO are structurally stable at 24 hours even after entering the nucleus (Fig. 3G and fig. S11). These results confirm the stability of 8HB in the cytoplasm and reveal that structures delivered into the nucleus also remain intact. Combined, our results indicate that the 8HB DO nanostructure is structurally stable after electroporation, for at least 24 hours when exposed in vitro to cytoplasmic and nuclear extracts, and remains stable for 24 hours after electroporation into U2OS cells both in the cytoplasm and in the nucleus.

Fluorescence imaging of DO in fixed U2OS cells

To assess the efficiency of the piggybacking approach via Pol II antibodies as a delivery method of fluorescently labeled DOs to cell nuclei, U2OS cells were electroporated with 8HB-8Cy5 conjugated to either zero antibodies (hereafter called 8HB-8Cy5), one anti–Pol II antibody (hereafter, called anti–Pol II 8HB-8Cy5 1Ab), or two anti–Pol II antibodies (hereafter called anti–Pol II–8HB-8Cy5 2Ab). We also tested 8HB-8Cy5 structures conjugated with one anti–maltose-binding protein (MBP) antibody that has no endogenous targets in human cells (hereafter called anti-MBP 8HB-8Cy5 1Ab) and 8HB with no Cy5 and no antibodies (hereafter called 8HB-No Cy5) as controls. U2OS cells were fixed, and nuclei were stained 24 hours after electroporation. Cells were imaged using HILO illumination. Hoechst nuclear stain was used to locate and focus on the mid-plane of the nucleus to visualize DO within the nuclear interior. The individual DO structures appeared as bright, diffraction-limited spots throughout the cytoplasm and within the nucleus (Fig. 4A), which were absent in negative controls in which cells were electroporated with buffer alone or with unlabeled DO (fig. S12). In addition to diffraction-limited punctate structures, we also observed large and bright spots mainly located within the cytoplasm (Fig. 4A), which likely correspond to aggregated DO structures. To determine the number of structures within the nucleus, we used a custom Fiji macro, which used the nuclear stain as a mask. Individual spots that fell within the mask and had intensity above a threshold value (see Materials and Methods) were counted as a DO particle, likely corresponding to an individual structure. Brighter spots could correspond to multiple structures in close proximity, but these were still counted as a single particle in our analysis. The number of particles was normalized by the nuclear area to determine the density of DO within each nucleus at the midplane (Fig. 4B). We found that the conjugation of one or two RNA Pol II antibodies to DO increased the overall number of 8HB-8Cy5 structures delivered to cell nuclei when compared to unconjugated DO or DO labeled with one anti-MBP antibody (Fig. 4B). The quantified densities correspond on average to 22, 105, and 96 DO particles at the nuclear midplane for the 8HB with 0, 1, or 2 anti–Pol II antibodies, respectively. These results

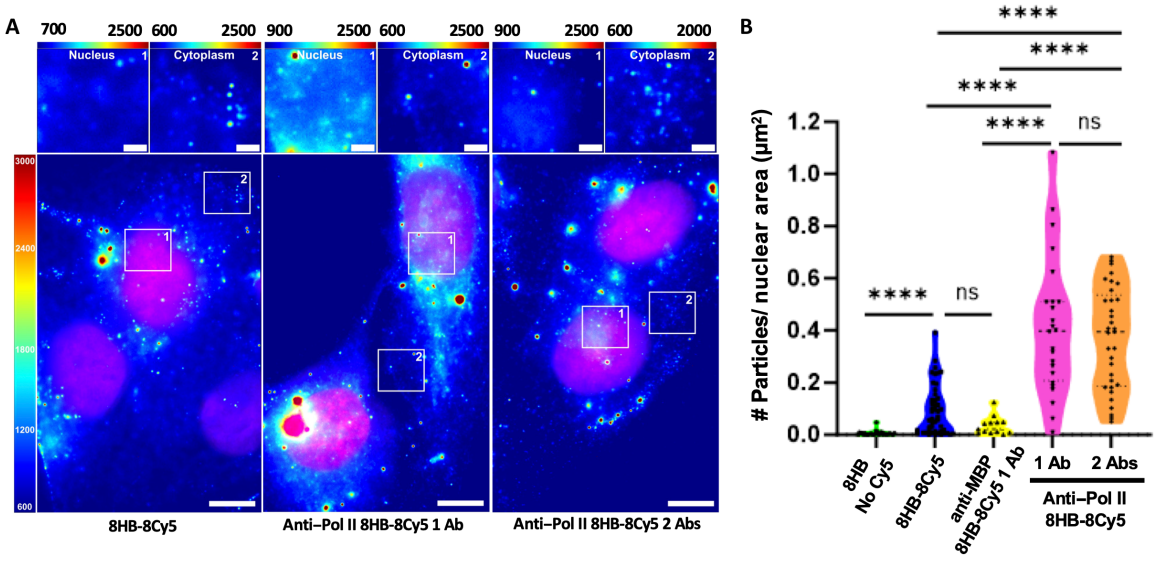

Fig. 4. Pol II antibodies facilitate the piggybacking of DOs to the nucleus. (**A**) HILO imaging at the mid-plane of U2OS cells illustrates DO structures inside cells for 8HB-8Cy5 with zero antibodies (left, 8HB-8Cy5), one Pol II antibody (middle, anti–Pol II 8HB-8Cy5 1 Ab), or two Pol II antibodies (right, anti–Pol II 8HB-8Cy5 2 Ab). A clear increase in Cy5 fluorescence emission in cell nuclei is evident when 8HB-8Cy5 are labeled with one or two Pol II antibodies. Upper images show zoomed-in views of the nucleus and the cytoplasm for each condition. Scale bars, 10 μm. (**B**) The number of observed particles in the nuclei was quantified for each condition, showing that some 8HB-8Cy5 enter the nucleus even without antibodies, and there is a significant increase in nuclear localization with one or two antibodies on 8HB-8Cy5 structures. ****$P \leq 0.0001$; ns, not significant.

were further confirmed via confocal imaging in which antibody–conjugated 8HB-8Cy5 were detected inside the nuclei in single z slices (fig. S13). U2OS cells typically divide every 24 to 26 hours. During our cell imaging experiments, we rarely observed dividing cells, which is likely because electroporation delayed cell cycle progression. Hence, the few dividing cells with nuclear envelope breakdown and reformation cannot solely account for relatively high proportion of the cells with nuclear DOs. Furthermore, our observation that the anti–Pol II antibody facilitates entry indicates that the DOs are being delivered via the piggybacking mechanism.

To estimate the efficiency of the piggybacking approach, we analyzed the anti–Pol II 8HB-8Cy5 spots observed in the cytosol. We focused this analysis on the smaller diffraction limited fluorescence spots that appeared to be single DO (fig. S14A). These smaller spots exhibited similar fluorescence intensity distribution to the spots observed in the nucleus (fig. S14B), both being a single peak distribution, consistent with them being individual structures. We counted the number of these singular DOs inside the nucleus and inside the cytosol. We found a ratio of 0.5 ± 0.6 (nuclear/cytosolic DO, average ± SD measured across 23 cells), suggesting that for the anti–Pol II 8HB-8Cy5 that remain as individual structures inside the cell, approximately 50% of them reach the nucleus.

Visualizing delivery of DO nanostructures into live-cell nuclei

To demonstrate the RNA Pol II–facilitated nuclear delivery of DO nanostructures in living human cells, we electroporated anti–Pol II antibody–functionalized 8HB-8Cy5 structures into U2OS cells. Since our prior results revealed no significant benefit to the incorporation of two anti–Pol II antibodies, we only performed live-cell experiments with the single antibody–conjugated DO (labeled as anti–Pol II 8HB-8Cy5 in Fig. 5, A to D). As controls, we also tested 8HB-8Cy5 linked with one anti-MBP (labeled as anti-MBP 8HB-8Cy5 in Fig. 5, A and B), as well as 8HB-8Cy5 with no antibodies (labeled as 8HB-8Cy5 in Fig. 5, A and B) or 8HB structures without any antibodies or Cy5 (labeled as 8HB-No Cy5 in fig. S15). Twenty-four hours after electroporation, nuclei were stained with Hoechst, and cells were imaged using live HILO microscopy with high temporal resolution (100 fps) for 10 s (movie S1). We first compared the number of 8HB-8Cy5 structures measured in the nucleus of live cells as observed from the nuclear Cy5 signals. To identify these nuclear signals, we used maximum intensity–projected images of five consecutive frames from the 210- to 250-ms time points from each sample. This revealed numerous diffraction-limited spots that appeared highly abundant in the case of the anti–Pol II 8HB-8Cy5 sample (Fig. 5A, left). Quantification of the number of particles revealed significant enrichment in cells electroporated with anti–Pol II 8HB-8Cy5 compared to all three control conditions (Fig. 5B and fig. S15). These results are consistent with our fixed-cell imaging results and show that 8HB DO structures functionalized with RNA Pol II–specific antibodies are targeted by piggybacking of endogenous Pol II to the nuclei of living human U2OS cells.

Live-cell imaging revealed clear motion of the Pol II–bound anti–Pol II 8HB-8Cy5 structures inside the nucleus as shown by the time-lapse recordings (movie S1). Comparing the anti–Pol II 8HB-8Cy5 to either the anti-MBP 8HB-8Cy5, the 8HB-8Cy5, or the 8HB no Cy5 revealed that mobile 8HB DO structures were not, or hardly, visible in the control cases (Fig. 5A and movies S1 and S2). For the Pol II–bound anti–Pol II 8HB-8Cy5 case, the motion of individual structures could be tracked over multiple frames (10 ms per frame), while the structures remained in the image plane. We tracked the motion of 161 individual anti–Pol II 8HB-8Cy5 structures (several example trajectories are shown in Fig. 5C). The length of these trajectories was limited to only a few tens of milliseconds due to the

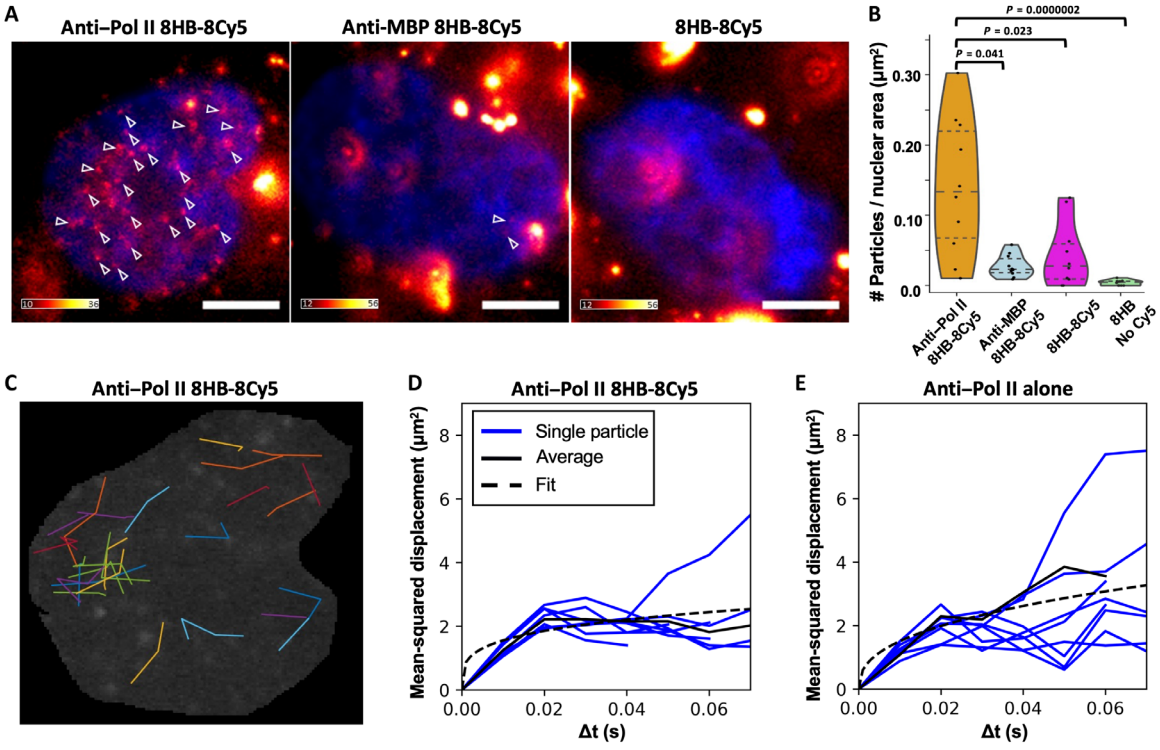

Fig. 5. Nuclear delivery of DOs in live cells. (**A**) Representative images of live U2OS cells 24 hours after electroporation with nonfunctionalized 8HB DO structures (right, 8HB No Cy5) or 8HB-8Cy5 DO structures functionalized with either one anti–Pol II antibody (anti–Pol II 8HB-8Cy5; left), one anti-MBP antibody (anti-MBP 8HB-8Cy5; second from left), or 8HB-8Cy5 with no antibodies (8HB-8Cy5; second from right). White arrowheads point to nuclear particles representing single DO structures. Color bars indicate the fluorescence intensity range of the Cy5 signal (scale is ×1000). Nuclear Hoechst staining is shown in blue. Scale bars, 5 μm. (**B**) Combined violin, box, and jitter plots showing the quantification of nuclear particles. A significantly higher number of particles per nuclear area were detected in cells that were electroporated with anti–Pol II 8HB-8Cy5 compared to the other three conditions ($H = 22.6447$, $P = 4.789 \times 10^{-5}$, Kruskal-Wallis test). *P* values for pairwise comparisons using Dunn post hoc analyses are shown. $n = 10$. (**C**) Traces of tracked particles for anti–Pol II 8HB-8Cy5 within the nucleus depicted in (A). (**D**) Average MSD data measured from each of the eight nuclei analyzed and power-law fit over the entire data showing anomalous diffusion with an exponent of 0.4 (95% CI 0.2 to 0.6). (**E**) Average *MSD* data for Alexa 647–labeled anti–Pol II antibody–Pol II complex (anti–Pol II alone), without DO, from eight nuclei as in (D), showing anomalous diffusion with exponent 0.5 (95% CI 0.2 to 0.8).

movement of particles out of the image plane. Nevertheless, calculating the mean squared displacement (MSD) over these short imaging periods as a function of time revealed that structures exhibit anomalous diffusion in nuclei following a power law behavior, $MSD \propto t^{\alpha}$, with a coefficient of $\alpha = 0.4$ [95% confidence interval (CI): 0.2 to 0.6] (Fig. 5D). This coefficient of $\alpha < 1$ indicates subdiffusive motion likely due to the crowded and viscoelastic nuclear environment. For comparison, we performed similar nuclear delivery imaging experiments and tracking analysis for the labeled anti–Pol II antibody alone piggybacked to the nucleus by endogenous Pol II (labeled anti–Pol II alone in Fig. 5E), which showed that the antibody–Pol II complex exhibited comparable subdiffusive motion with a similar coefficient of $\alpha = 0.5$ (95% CI: 0.2 to 0.8) (Fig. 5E). The MSD fits revealed diffusion coefficient factors of 12.6 $\mu m^2/s$ (95% CI: 1.5 to 23.8) and 9.5 $\mu m^2/s$ (95% CI: 3.8 to 15.2) for the anti–Pol II 8HB-8CY5 and the anti–Pol II alone, respectively. These results indicate that the anti–Pol II 8HB-8CY5 moves similarly to the anti–Pol II antibody once inside the nucleus. The lower α coefficient of the anti–Pol II 8HB-8Cy5 case suggests that the additional size of the DO could cause greater hindrance to motion of the attached antibodies and attached Pol II within the nucleus, but more careful analysis of the intracellular motion of these constructs would require tracking particles for longer periods of time with three-dimensional (3D) particle tracking. These particle motion tracking results are also consistent with the subdiffusive motion of other nuclear factors like the transcription factor P-TEFb, which was previously reported to exhibit a power law coefficient of $\alpha = 0.6$ inside the nucleus (*46*).

DISCUSSION

DO nanostructures have been demonstrated for applications like biophysical measurements (*8*, *47*), manipulating molecular interactions (*9*, *10*), and delivery of therapeutic agents (*2*, *7*, *48*), which could all be useful intracellular functions; other applications like high-resolution imaging (*22*), nucleic acid and protein detection (*2*, *49*), probing of chromatin substructures (*28*, *29*), and gene delivery (*14*–*16*) could particularly benefit from mechanisms to specifically deliver DO to live-cell nuclei. As a critical step for intracellular delivery and applications, we evaluated the stability of DOs in relevant conditions including cell culture media, cell cytoplasmic and nuclear extracts, upon electroporation, and inside cells. Our results show that the DO designs used here are stable in cell media and in nuclear and cytoplasmic extracts for 24 hours, which is consistent with prior work showing that DO can exhibit extended stability in cell culture

or in cell lysates (*36*, *50*, *51*). The stability is design dependent, and DO can degrade more rapidly at higher serum levels (*52*, *53*), which is an important consideration especially for translational applications. However, multiple strategies exist such as ultraviolet (UV) cross-linking or polymer coating and brushes that can extend the stability of DOs (*54*–*56*). Prior work has shown that the process of electroporation can affect structural integrity of DO (*57*), while others studies have demonstrated that some DO designs can remain stable through electroporation (*14*, *15*), suggesting that the electroporation stability is dependent on the design and electroporation parameters. Our results show that the 8HB DO structure and antibody attachment is stable after electroporation. We also demonstrate that the 8HB DO can remain stable for 24 hours after electroporation into cells in the cytoplasm or after entering the nucleus. While prior work has not evaluated DO inside nuclei, our results are in agreement with prior studies showing that some DNA nanostructure designs can exhibit extended stability inside cells (*58*–*60*).

Several prior efforts have studied interactions between DO and cells [e.g., see recent reviews (*12*, *61*)], and a few recent studies have demonstrated effective delivery of gene sequences folded into DO structures where genes can be expressed (*14*–*16*, *32*). Two of these studies leveraged either Cas9 (*14*) or an SV40-derived DNA sequence (*32*) to promote delivery to the nucleus. However, these studies were focused on delivering information through the DNA sequence to the nucleus rather than intact DO structures. Unlocking potential device functions of DO inside cell nuclei requires methods that allow for the delivery and tracking of intact DO into live cells and targeted delivery to nuclei. Here, we targeted DOs to the nucleus by functionalizing them to bind neosynthetized nuclear factors in the cytoplasm, in this case, the largest subunit of the RNA Pol II. As the nuclear factor is imported to the nucleus, the DO can be carried, or piggybacked, along with them.

We found that this piggybacking approach is size dependent, with no clear nuclear delivery observed using a larger size DO (~4.8 MDa, ~90-nm-long nanorod), while the piggybacking approach worked effectively to deliver smaller structures (~0.5 MDa, ~30-nm-long nanorod) to the nucleus. We confirmed that these DO remain intact inside cells for 24 hours using two-color fluorescence colocalization (DO dual-labeled with Cy3 and Cy5), including comparison to codelivery of single-labeled structures (Cy3-labeled DO plus Cy5-labeled DO) to verify that colocalization is the result of intact structures (*45*). iSIM imaging further revealed that DO can remain intact in live-cell nuclei 24 hours after electroporation, hence opening a door to leverage the diverse functions of DO inside the nucleus. Our fluorescence colocalization studies confirm that the overall structure remains intact inside cells and nuclei; however, it is possible that there may be local degradation such as nicking of strands that might affect local structure. Hence, it may still be important for future studies to verify the stability of local structural features or properties for specific applications. These ~30-nm-nanorod DO already provide a useful basis for functions like imaging or detection with the simple inclusion of fluorophores or aptamers (*62*). Our results further showed that these DO are mobile inside the nucleus. They exhibit subdiffusive motion similar to what has previously been measured for other nuclear factors (*46*), which is likely due to the highly constrained environment inside the nucleus. Nevertheless, our results suggest that the piggybacked DO can explore the nuclear volume and that the anti–Pol II 8HB-8Cy5 exhibits similar motion in the nucleus to antibody-bound Pol II complex alone. Our results further showed that ~50% of individual anti–Pol II 8HB-8Cy5 structures reached the nucleus within 24 hours. Prior nuclear delivery experiments with the same anti–Pol II antibody alone in U2OS cells revealed that the full antibody (~150 kDa) started entering the nucleus after several hours and the large majority reached the nucleus within ~24 hours, while smaller Fab fragments (~50 kDa) were fully nuclear within 6 hours (*33*). Comparing to our findings suggest that the DO cargo may slow down trafficking of the anti–Pol II antibody to the nucleus and that smaller DO likely traffic to the nucleus faster, but future studies will be required to better understand how DO design parameters affect the kinetics of trafficking and delivery efficiency across multiple cell types.

Some functions of DO would likely be enhanced through the use of a variety of DO structures. On the basis of our results, DO designs similar in size to the 8HB (~30 nm in length and ~6 nm in cross-sectional dimensions, ~0.5 MDa) or smaller should also be delivered to nuclei using the piggybacking approach. For applications that require larger structures, we found that the 26HB structure (~90 nm in length and ~10-15 nm in cross-sectional dimensions, ~4.8 MDa) did not enter the nucleus. However, a key factor limiting the use of this larger 26HB DO was aggregation in the cytoplasm. It is unlikely that the dimensions of the 26HB are prohibitive to nuclear entry since the nuclear pore complex can accommodate larger objects like HIV particles (*63*). It is also possible that the aggregates we observed are interacting with organelles or intracellular vesicles, which could inhibit their trafficking. DO design modifications, such as surface-coating approaches (*54*), that reduce intracellular aggregation or modulate interactions with cellular components could allow for these larger structures to enter the nuclei. We further found that labeling DOs with two anti–Pol II antibodies did not provide any advantage relative to a single anti–Pol II antibody. Since the antibody targets the heptapeptide repeat sequences at the C-terminal domain of the largest subunit of Pol II, it is likely that two antibodies can bind a single Pol II. This suggests that the affinity of DO binding to Pol II was not a limiting factor for the 8HB, but it is still possible that multiple targeting moieties may be helpful for larger structures or different target molecules. More broadly, the large design space of DO in terms of size, shape, surface coating, and functionalization can likely enable engineering of intracellular behaviors such as aggregation, passive or active transport, and entry to the nucleus or other cell compartments. Our results and other recent efforts (*12*, *14*, *32*, *45*, *58*, *60*) provide a framework to guide these studies. In the future, a better understanding of these intracellular behaviors of DO will be important to for enabling additional applications, for example, those that leverage multicomponent devices like biophysical measurements (*28*).

The piggybacking approach we presented here relies on binding neosynthetized nuclear factors in the cytoplasm that will be imported to the nucleus. Here, we targeted the RNA Pol II building on prior studies that established the piggybacking approach for delivering antibodies to the nucleus (*33*–*35*). These studies used the same approach to visualize multiple transcription factors, including TATA-binding protein (TBP) and TBP-associated factor 10 (TAF10) in the nuclei of human cells, and showed that anti–Pol II antibodies can be delivered to the nucleus in multiple cell types (e.g., U2OS, HeLa, HFF-1 fibroblasts, and *Drosophila* Schneider S2 cells) demonstrating the versatility of the antibody piggybacking approach. This suggests that these transcription factors, and likely a variety of other nuclear factors, could be used to piggyback DO

structures to the nucleus. These proteins have specific mechanisms that drive localization to the nucleus, such as interactions with other proteins [e.g., RNA Pol II–associated protein, RPAP2 (*64*)] that mediate trafficking or direct interactions with importins via nuclear localization signal (NLS) sequences or other domains (*65*). Prior studies showed that the expression of gene sequences delivered via DO is increased with inclusion of either amino acid NLS or DNA nuclear targeting sequences (DTS) (*14*, *32*). Combined with our results, these studies suggest that a variety of proteins or motifs or direct inclusion of NLS or DTS sequences onto DO could be alternative routes to specifically deliver intact DO devices to the nucleus.

MATERIALS AND METHODS

Design and simulation of DO nanostructures

To achive the delivery of DOs to the nuclei of live cells, we initially tested two DO designs, an 8HB, which is 30-nm long with a molecular weight of ~0.5 MDa, and a 26HB, which is approximately 90-nm long with a molecular weight of ~4.8 MDa. Prior research has demonstrated the efficient folding and stability of the 26HB in cell culture media, as well as its effective cellular uptake (*36*, *39*) and the 8HB design uses a similar but smaller square lattice cross section. We used a previously reported design for the 26HB structures (*36*, *37*, *39*). The 8HB nanostructure was designed in caDNAno (*38*) (fig. S16 and table S1, design available on nanobase.org, https://nanobase.org/structure/237) using a hollow square-lattice cross section (*66*). The staple strand routing was designed to contain ideally one long continuous duplex region per strand, which has been shown to facilitate robust folding (*67*, *68*). The scaffold routing was designed to contain a seam near the middle of the bundle, which has been shown to inhibit isomerization of the structure (*4*, *69*). Coarse-grained MD simulations were performed using the oxDNA model (*40*, *41*, *70*) after converting the caDNAno output files through tacoxDNA (*71*) into oxDNA topology and configuration files. Initial relaxation was performed using default parameters (oxdna.org). Simulations were run for 100,000,000 steps, and the mean over the full trajectory was used to depict the 8HB structure in Fig. 2, A and C. For the depiction of 8HB with overhangs and antibody, the relaxed structure was converted to an all-atom Protein Data Bank (PDB) representation and visualized alongside a PDB representation of antibody (1igt) in ChimeraX (*72*) for scale.

Production of ssDNA scaffolds

Scaffold strands (769-nt; sequence in table S2) were produced through polymerase chain reaction (PCR) using one 5′ phosphate modified primer to allow exonuclease digestion after PCR (*73*, *74*). The ssDNA scaffold was initially prepared using Guide-it Long ssDNA Production System v2 kit (Takara Bio, 632666) following the manufacturer's protocol. Subsequent larger-scale preparations were performed using PCR followed by lambda exonuclease digestion. Briefly, the target scaffold sequence was first amplified in double-stranded DNA (dsDNA) form via PCR from M13mp18 using PrimeSTAR Max Premix (Takara Bio, R045A) and 0.8 μM primers (Integrated DNA Technologies, primer sequences in table S3), where the reverse primer is modified with 5′ phosphate to facilitate selective exonuclease digestion. The PCR product was then mixed with 1/3 volume of 10 M ammonium acetate (Sigma-Aldrich, A1542) and 2 volume of ethanol (Sigma-Aldrich, E7023) to perform EtOH precipitation (*75*), and the dsDNA pellet was resuspended in 5 mM tris in ddH_2O. To digest the anti-sense strand, dsDNA was mixed with lambda exonuclease (New England Biolabs, M0262) in the vendor-supplied buffer, adjusted to 250 ng/μl DNA concentration, and then incubated at 37°C for 6 hours. One-unit lambda exonuclease was added per 30 μg of DNA. After digestion, 10 mM EDTA was added to quench the reaction followed by heat inactivation at 75°C for 10 min. Digested ssDNA product was then mixed with 1 μl of glycogen (20 mg/ml; Thermo Fisher Scientific, R0561) and 1/3 volume of 10 M ammonium acetate to perform EtOH precipitation, and the ssDNA pellet was resuspended in 1× TE buffer [10 mM tris-HCl (pH 8.0) and 1 mM EDTA]. Resuspended ssDNA was evaluated using gel electrophoresis on 1.5% agarose gel in 1× TAE buffer (40 mM tris base, 10 mM acetic acid, and 1 mM EDTA) (fig. S17).

Folding and purification of DO nanostructures

DO nanostructures were folded according to established protocols (*76*–*78*). Briefly, 20 nM scaffold ssDNA was mixed with a 10-fold excess of staple strands in folding buffer (5 mM tris, 1 mM EDTA, 5 mM NaCl, and 20 mM $MgCl_2$) and subjected to thermal annealing (Bio-Rad C1000 Thermocycler). Details of the thermal annealing protocol can be found in the Supplementary Materials (table S4). Agarose gel electrophoresis was used to evaluate the folding of the DO nanostructures. Agarose gels (2% agarose, 0.5× TAE with 10 mM $MgCl_2$, containing 0.5 μg/ml ethidium bromide) were run for 90 min at 90 V cooled in an ice-water bath or in a 4°C refrigerator. For nuclear delivery experiments structures were purified by centrifugation in the presence of polyethylene glycol (PEG) (*79*). Briefly, the solution of folded DO was mixed with an equal volume of 15% PEG8000-based precipitation buffer and spun at 16,000*g* for 25 min to pellet DO. The pellet was resuspended in desired buffer to recover DO after discarding supernatant (SN) containing excess staple strands.

After purification through two rounds of centrifugal PEG precipitation, the DO was resuspended in 1× phosphate-buffered saline (PBS) with 2.5 mM $MgCl_2$, and the concentration was measured using a Nanodrop (Thermo Fisher Scientific, ND-ONEC-W). To label DO with fluorophores, the structures were designed to contain eight ssDNA overhangs (i.e., staples that protrude from the bundle structure) to allow for binding complementary oligonucleotide strands containing a Cy5 fluorophore label (sequences in table S1). Fluorophore-labeled strands were designed to bind, so the fluorophore is located near the surface of the structure. Fluorophore-labeled strands were incubated with the structures at 20-fold molar excess with respect to the DO concentration. This excess corresponds to a 2.5-fold molar excess relative to the number of overhang strands on the origami structures. The mixture was then incubated at 37°C for 2 hours to allow for efficient binding of the fluorophore-labeled staples. The excess fluorophore-labeled overhangs were removed using a 0.5-ml 100-kDa molecular weight cutoff (MWCO) Amicon filter unit by loading the sample into the filter unit (the total volume does not exceed the 0.5-ml capacity of the filter) and centrifuging at 2000*g* speed for 5 min. This filtration step was repeated five times with the addition of PBS buffer containing 2.5 mM $MgCl_2$ buffer into the filter unit, which ensured the elimination of excess fluorophore-labeled staple strands. The purified nanostructures were then stored at 4°C for subsequent antibody labeling.

Antibody preparation

The mouse monoclonal antibody (mAb 7G5) specific for the C-terminal repeat domain (CTD) of the largest subunit of Pol II, RPB1-CTD (hereafter called anti–Pol II antibody), and the mouse monoclonal antibody (17TF2-1H4) specific for the bacterial MBP (anti-MBP, #MA3045 Thermo Fisher Scientific) were purified as described (*34*), with minor modifications. MBP is not expressed in mammalian cells and hence provides a nonspecific antibody control. Briefly, 1 ml of antibody-containing ascites was incubated with 1.2 ml of settled bead volume of preequilibrated Protein G Sepharose Fast Flow beads (GE Healthcare) for 2 hours at 4°C with gentle agitation. Beads were then transferred to a Poly-Prep Chromatography column (Bio-Rad) and washed for 20 column volumes with PBS. Antibodies were eluted in 1 ml of fractions by 0.1 M glycine (pH 2.7) and were directly neutralized with 70 to 90 μl of 1 M tris-HCl (pH 8.0). Aliquots (6.5 μl) from each fraction were analyzed by SDS–polyacrylamide gel electrophoresis (SDS-PAGE), and the fractions containing most of the antibodies were pooled and dialyzed in DiaEasy Dialyzer 6 to 8 kDa MWCO dialysis tubes (K1013-100, BioVision) against 2 liters of PBS overnight and then for 2 hours with 2 liters of fresh PBS. The antibody solution was then concentrated on Amicon Ultra-4 centrifugal filters with 10 or 50 kDa MWCO (Millipore) to 1 to 4 mg/ml in PBS.

Conjugation of antibodies with DNA

To initiate the process of DNA-antibody conjugation, 2 μl of DBCO-PEG5-TFP cross-linker (dissolved in dimethyl sulfoxide to a concentration of 900 μM) was combined with purified anti–Pol II antibody (or anti-MBP antibody, 1 mg/ml) in 100 μl of PBS buffer (pH 7.4). The mixture was then incubated at 37°C with gentle shaking for 4 hours. Following this, the antibody-crosslinker product was removed through dialyzing for three times against 4 liters of PBS with a 6- to 8-kDa MWCO dialysis membrane. The first two dialysis were done for 2 hours, while the third was done overnight.

Subsequently, the purified antibody-crosslinker product was combined with a twofold excess of azide-modified oligonucleotide (sequences in table S1) in PBS. The mixture was incubated at 37°C with gentle shaking for 2 hours, followed by incubation at room temperature overnight. To remove excess azide oligos, the sample was buffer exchanged five times into PBS with 2.5 mM $MgCl_2$ with a 0.5-ml 100-kD MWCO Amicon filter unit. The resulting purified DNA-conjugated antibody was then stored at 4°C for DO functionalization. The DNA-conjugated antibodies were analyzed by SDS-PAGE to confirm conjugation (fig. S18).

Functionalization of antibody-labeled DO

To conjugate DNA-labeled antibodies to DO, a solution containing 1 μM DNA-antibody conjugates was added to a solution of 100 nM fluorophore-labeled DO structures in a 100-μl buffer of 1× PBS containing 2.5 mM $MgCl_2$. The mixture was thoroughly mixed and incubated at 37°C with gentle shaking for 2 hours and then at room temperature overnight. The conjugation of the antibodies to the structures was confirmed with agarose gel electrophoresis [2% agarose, 0.5× TAE buffer, 10 mM $MgCl_2$, and ethidium bromide (0.5 μg/ml)] for 180 min at 90 V (fig. S3). Samples for TEM imaging were purified using the Freeze 'N Squeeze (Bio-Rad) gel extraction column as per the manufacturer's protocol. The target bands were excised from agarose gels, placed into the respective spin columns, and spun at 10,000*g* for 5 min.

Purification of antibody-labeled DO

All DO samples used in cellular experiments were purified via gel electrophoresis with electroelution to obtain a pure product of DO labeled with zero, one, or two antibodies. The agarose gel [2% agarose, 0.5× TAE buffer, 10 mM $MgCl_2$, and ethidium bromide (0.5 μg/ml)] electrophoresis was done for a duration of 180 min at 90 V while cooled in an ice bath or in a 4°C refrigerator. The desired bands were excised from the gel and placed in a dialysis membrane containing the same running buffer. The DO sample was then electroeluted from the gel fragment with a constant voltage of 90 V was applied for 1 to 2 hours until the product of interest had migrated out of the gel fragment and into the buffer as confirmed by the absence of ethidium bromide signal. The voltage was then reversed for 1 to 2 min to release any DO sample that was bound to the dialysis membrane. The DO sample was recovered from the dialysis membrane with a syringe and filtered through a 0.2-μm filter to remove any remaining agarose. Last, the DO sample was concentrated and buffer exchanged into 1× PBS with 2.5 mM $MgCl_2$ using an Amicon filter with 100-kDa MWCO.

TEM imaging of DO structures

Samples for TEM imaging were prepared as previously described (*76*, *80*). Briefly, the DO sample was diluted to a concentration of 1 to 2 nM in 1× PBS containing 2.5 mM $MgCl_2$. A glow-discharged copper grid was placed on a 10-μl drop of the DO sample on a parafilm sheet. The grid was incubated on the sample droplet for 4 to 6 min at room temperature to allow the DO structures to deposit onto the surface. Excess sample was removed by gently dabbing the edge of the grid with a piece of filter paper (Whatman). To stain the grid, two 10-μl drops of 2% uranyl formate solution were deposited on a parafilm sheet. The first drop was applied onto the grid and immediately dried by gently dabbing the edge of the grid onto a piece of filter paper. The second drop was applied onto the grid and incubated for 5 to 10 s. Excess stain was then removed from the grid by again gently dabbing the edge of the grid with a piece of filter paper. The grid was allowed to dry for at least 20 min before imaging. TEM imaging was performed at the OSU Campus Microscopy and Imaging Facility on an FEI Tecnai G2 Spirit TEM using an acceleration voltage of 120 kV.

Stability of DO in cell culture media

Cy5-labeled DO samples were prepared at a concentration of 50 nM. Subsequently, 4 μl of each DO structure was mixed with 6 μl of the cell culture media (details of media provided in Cell Culture section). The mixture was incubated at 37°C for varying time periods (0, 1, 3, 6, 8, 12, and 24 hours). To provide a baseline for comparison, a control sample of DO in 1× PBS with 2.5 μM $MgCl_2$ buffer was prepared. For each time point, all samples, including the control, were evaluated by gel electrophoresis (2% agarose gel in 0.5× TAE buffer with 10 mM $MgCl_2$ without ethidium bromide) run at 90 V for 90 min cooled in an ice water bath or deli refrigerator. The resulting gel was imaged in a Cy5 channel, followed by post staining with ethidium bromide (0.5 μg/ml) and imaging with UV excitation on a gel imager system (UVP GelStudio by Analytik Jena). The integrity of DO structures of different

sizes over time were assessed by comparing the gel electrophoretic mobility to their respective control sample. In addition, high-resolution TEM images of the DO structure were to further evaluate their structural stability. The samples were purified for TEM imaging using the Freeze 'N Squeeze (Bio-Rad) gel extraction column, and imaging samples were prepared as previously described.

Stability of DO in nuclear and cytoplasmic extracts

A volume of 4 μl of Cy5-labeled DO structures at 50 nM concentration was mixed with 6 μl of U2OS cytoplasmic and nuclear extracts both at 1 μg/μl (AscentGene) for a final DO concentration of 20 nM. The mixtures were incubated at 37°C for varying time periods (0, 1, 3, 6, 8, 12, and 24 hours). After these incubations, the structural integrity of the DO was evaluated using both gel electrophoresis (a 2% agarose gel in 0.5× TAE buffer with 10 mM $MgCl_2$) run for 90 min at 90 V cooled in an ice bath or at 4°C in a refrigerator. Structures were also evaluated by TEM to confirm structural stability following gel purification using Freeze 'N Squeeze (Bio-Rad) gel extraction columns.

Stability of DO after electroporation

A volume of 4 μl of Cy5-labeled DO structures at 50 nM concentration were mixed with 6 μl R buffer solution (Neon kits-MPK1096, Thermo Fisher Scientific). DO structures in R buffer were then immediately subjected to electroporation using the Neon Transfection system (MPK5000, Thermo Fisher Scientific) under the same conditions as cellular experiments using the 10-μl Neon tips with the following parameters: 1550 V, 3 pulses, and 10 ms per pulse. A control sample of each structure was also prepared in 1× PBS with 2.5 μM $MgCl_2$ buffer for comparison, and DO structures in R buffer solution but without electroporation were also examined as a control. The stability of the DO structures was characterized using gel electrophoresis and TEM imaging, as described above.

Cell culture

A human osteosarcoma U2OS cell line (ATCC HTB-96) was obtained from the American Type Culture Collection (Manassas, VA). Cells were maintained in 5% CO_2 atmosphere at 37°C in Dulbecco's modified Eagle's medium (DMEM) (4.5 g/liter glucose) supplemented with 2 mM GLUTAMAX-I, 10% fetal calf serum (FCS), penicillin (100 UI/ml), and streptomycin (100 μg/ml).

Electroporation of DO into cells

Electroporation was performed using the Neon Transfection system with the 10-μl Neon electrode tips (MPK5000 and MPK1096, Thermo Fisher Scientific) according to the manufacturer's instructions. U2OS cells were washed once with Dulbecco's PBS (DPBS, 14190136; Gibco) and then trypsinized (0.25% trypsin-EDTA; 25200-056; Gibco) for 3 min at 37°C. Cells were then resuspended in R buffer to obtain 10^5/10 μl cell suspension. Cells (10^5) were mixed with 2 μl of 50 nM origami constructs and electoporated in the electrode tips using the following settings: 1550 V, 3 pulses, and 10 ms per pulse. The electroporated sample was then transferred directly into one well of an eight-well microscopy slide (Nunc Lab-Tek II for wide-field imaging) containing 300 μl of prewarmed medium without antibiotics and was incubated for 24 hours in 5% CO_2 atmosphere at 37°C.

Flow cytometry

U2OS cells were electroporated with 8HB-8Cy5 DOs or mock electroporated (i.e., electroporation buffer with no DO) as described above. For flow cytometry analyses, two electroporations of each sample were pooled and seeded in a well of a 24-well plate in 600 μl of medium. Twenty-four hours later, the cell culture SNs were collected, and then cells were harvested and pooled with their corresponding SNs and stained with DAPI (200 ng/ml; Sigma-Aldrich, #MBD0016-1ML) for 10 min before passing them on a BD FACSymphony A1 flow cytometer (DB Biosciences). Fluorescence data were collected on the forward scatter (FSC) and side scatter (SSC); the DAPI and Cy5 fluorophores were excited using the violet (405 nm) and red (637 nm) lasers, respectively, and fluorescence was collected using 450/50 plus 410LP and 670/30 plus 655LP filters, respectively. For flow cytometry data analyses, singlet events were first gated using FSC-area versus FCS-height scatter plots (typically ~90% single events). From these single events, DAPI-negative single live cells were gated on a DAPI versus FSC-area scatter plots. The DAPI-negative gate was set on the basis of unstained control cells. The gated live single cells were further analyzed on Cy5 histograms, where the Cy5-positive gate was set on the basis of Cy5-negative nonelectroporated U2OS control cells.

Sample fixation and staining for imaging of DO in fixed cells

U2OS cells were fixed 24 hours after electroporation with 4% paraformaldehyde solution for 10 min at 37°C, rinsed with DPBS, and subsequently incubated with (1:10,000) Hoechst 33342 trihydochloride, trihydrate (H3570; Invitrogen) stain solution in DPBS for an additional 10 min at room temperature and covered. Cells were rinsed again with DPBS and stored at 4°C until imaged.

Fluorescence imaging of fixed cell samples

Cells were evaluated by HILO imaging with the Oxford Nanoimager S microscope [100× oil immersion objective, 1.45 numerical aperture (NA), Hamamatsu Orca flash 4.0 CMOS camera, 200-ms exposure time]. The HILO illumination angle allows for wide-field imaging within cell nuclei while reducing background. DPBS storage buffer was exchanged for an oxygen-scavenging imaging buffer [GLOX- 14 mg glucose oxidase, catalase (20 mg/ml), 10 mM tris (pH 8.0), 50 mM NaCl, and 10% glucose in DPBS]. Healthy, Hoechst-stained nuclei that expressed punctate Cy5 signal were identified and imaged sequentially (10 frames at 200-ms exposure for each target) with excitation by 640-nm laser (origami labeled with 8× Cy5) followed by 405 nm (nuclei) in the same field of view and *z* position. For two-color experiments (origami labeled with 4× Cy3 and 4× Cy5) cells were also imaged under the same exposure conditions under excitation with 560 nm before 405 nm.

Confocal fluorescence imaging of fixed cell samples

Localization of 8HB DO in cells was also assessed by confocal microscopy. Fixed cell samples were imaged at 60× magnification using VT-iSIM high-speed super-resolution imaging system (VisiTech International) equipped with Olympus IX71 inverted; super-resolution VT-iSIM scan head; Hammamatsu ORCA Quest qCMOS camera; and 405-, 442-, 488-, 514-, 561-, and 640-nm excitation lasers. This system is best optimized for fast high-resolution confocal imaging of live or fixed samples. Image acquisition was set at the middle of the sample based on Hoeschst staining, and Z-stacks of 5 μm of total thickness were acquired with 0.2-μm step

size. Images were deconvoluted with microvolution plugin in ImageJ software.

Processing of fixed-cell images

Imaging data for all fixed-cell experiments were processed using an in-house FIJI (*81*) macro. In brief, final images used for analysis were projections of the average fluorescence intensity over 10 separate frames of the same field of view (200-ms exposure). The image plane was selected by identifying the plane of largest nuclear area based on Hoechst signal.

Analysis of nuclear delivery experiments

An in-house FIJI (*81*) macro was used to segment the nuclear region in images based on Hoechst signal and detect the fluorescent signal of DOs within the segmented nuclear area. In brief, the Hoechst images were first segmented by Gaussian blur (sigma 8.0) and then thresholded using Otsu's method (*82*). Thresholded nuclei were then made into regions of interest (ROIs), and their areas were measured. To quantify the origami signal, first, a flat background fluorescence value was subtracted from all origami images based on the maximum background fluorescence found in control images in which no origami was present. Then, each nuclear ROI was used as a mask on its respective origami image to segment the origami signal within that nucleus. Origami structures with high enough fluorescence signal above the background were detected and counted using the Find Maxima function (prominence = 60) within these ROIs after application of Gaussian blur (sigma 4.0). For each nucleus, the origami count was divided by the nuclear area.

Analysis of two-color delivery experiments

Colocalization of fluorescent signal in stability experiments was assessed with FIJI via JaCoP (Just another Colocalization Plugin) (*83*). In brief, fluorescent signal from origami labeled with Cy3, Cy5, or both fluorophores were thresholded using Otsu's method (*82*), and the degree of colocalization between signals was calculated as the Pearson's correlation coefficient.

Live-cell imaging of DO in cells

For live-cell imaging, 24 hours after electroporation, the medium of the electroporated U2OS cells on the eight-well microscopy slides was exchanged with 300 μl of fresh medium containing Hoechst33342 (500 ng/ml; H3570, Invitrogen) and no phenol red. After the medium change, cells were incubated for at least 10 min before imaging. The medium was then exchanged with 200 μl of live imaging–compatible oxygen quenching buffer [DMEM without phenol red containing glucose (22 mg/ml), 67.3 mM Hepes (pH 8.0), glucose oxidase (560 μg/ml; G2133, Sigma-Aldrich), and catalase (40 μg/ml; C1345, Sigma-Aldrich)], and cells were imaged immediately after adding the imaging buffer for no longer than 30 min on a HILO microscope.

HILO live-cell imaging was performed on a home-built setup [system details previously described (*84*)] based on a NikonEclipse Ti microscope equipped with an acousto-optic tunable filter (Opto-Electronic), a 100× 1.49-NA oil-immersion objective, and a Hamamatsu electron multiplying charge-coupled device (EM-CCD) camera (ImagEM X2 C9100-23B). Samples were imaged using a temperature-controlled on-stage chamber set to 37°C. The laser lines at 405 and 642 nm were used for excitation of Hoechst33342 and Cy5 fluorophores, respectively. Laser power during the experiments was set to 130 mW for the 642-nm laser. Z-stabilization was ensured by the perfect focus system (Nikon Eclipse Ti) on the microscope. EM-CCD gain was set to 610, and samples were imaged with 10 ms of exposure time over a total time of 10 s. After each time lapse, a single image of the nucleus based on Hoechst signal was also recorded in the 405 channel to identify the nuclear region.

Live-cell imaging data processing and analysis

Snapshots of live-cell time lapses were generated and analyzed in FIJI. First, maximum intensity projections of five consecutive frames of the Cy5 channel after the 20th (200 ms) frames were generated for each time lapse. For the example images shown in Fig. 5A, the Cy5 channel (shown in Red Hot LUT) was merged with the Hoechst image (shown in blue). For quantification (Fig. 5B), the nuclei were segmented on the basis of the Hoechst images, and the particles on the Cy5 images were detected inside the nuclear regions using the Detect Particle function of the ComDet v.0.5.5 plugin (https://github.com/UU-cellbiology/ComDet) with the following parameters: Do not Include larger particles; do not Segment larger particles; Approximate particle size: three pixels; Intensity threshold (in SD): 5; ROIs shape: ovals. The detected particles were then visually curated and counted. For the statistical analyses, a Kruskal-Wallis test with Dunn post hoc analyses were performed in Python 3.11.5 (packages scipy and scikit_psthocs).

For tracking the motion of DO structures, the live-cell imaging sequences were first processed in FIJI (*81*) to correct for photobleaching. Plane correction from the BioVoxxel package (*85*) was used to flatten the signal. The Hoechst stain for each sample was used to determine the nuclear region, and the origami signal outside of the nucleus was removed. A custom CellProfiler pipeline was used to identify individual DO structures and obtain persistent particle tracks. Custom MATLAB scripts (codes are available at https://github.com/marcello-deluca/nuclear-origami-live-imaging-analysis) were used to calculate the diffusive behavior of the DO structures based on MSD

$$MSD(\Delta t) = \frac{1}{n_{\mathrm{conf}} - \Delta t} \sum_{t=1}^{n_{\mathrm{conf}}-\Delta t} |\,\mathbf{R}(t+\Delta t) - \mathbf{R}(t)\,|^2$$

where Δt is the quantity of elapsed time (expressed in frames), n_{conf} is the overall number of configurations (frames) in a trace, t is a frame in the trace, and $\mathbf{R}$ is the 2D location of the origami at the specified frame of the trace determined in pixels and converted to nanometers based on a pixel size of 106.67 nm per pixel.

Supplementary Materials

This PDF file includes:

Figs. S1 to S18
Table S4
Legends for movies S1 and S2
Legends for tables S1 to S3

Other Supplementary Material for this manuscript includes the following:

Tables S1 to S3
Movies S1 and S2

REFERENCES AND NOTES

1. D. Yang, M. R. Hartman, T. L. Derrien, S. Hamada, D. An, K. G. Yancey, R. Cheng, M. Ma, D. Luo, DNA materials: Bridging nanotechnology and biotechnology. *Acc. Chem. Res.* **47**, 1902–1911 (2014).

2. Z. He, K. Shi, J. Li, J. Chao, Self-assembly of DNA origami for nanofabrication, biosensing, drug delivery, and computational storage. *iScience* **26**, 106638 (2023).
3. W. Ma, Y. Zhan, Y. Zhang, C. Mao, X. Xie, Y. Lin, The biological applications of DNA nanomaterials: Current challenges and future directions. *Signal Transduct. Target Ther.* **6**, 351 (2021).
4. P. W. K. Rothemund, Folding DNA to create nanoscale shapes and patterns. *Nature* **440**, 297–302 (2006).
5. S. Dey, C. Fan, K. V. Gothelf, J. Li, C. Lin, L. Liu, N. Liu, M. A. D. Nijenhuis, B. Saccà, F. C. Simmel, H. Yan, P. Zhan, DNA origami. *Nat Rev Methods Primers* **1**, 13 (2021).
6. M. DeLuca, Z. Shi, C. E. Castro, G. Arya, Dynamic DNA nanotechnology: Toward functional nanoscale devices. *Nanoscale Horiz.* **5**, 182–201 (2020).
7. Y. Zhang, X. Tian, Z. Wang, H. Wang, F. Liu, Q. Long, S. Jiang, Advanced applications of DNA nanostructures dominated by DNA origami in antitumor drug delivery. *Front. Mol. Biosci.* **10**, 1239952 (2023).
8. E.-C. Wamhoff, J. L. Banal, W. P. Bricker, T. R. Shepherd, M. F. Parsons, R. Veneziano, M. B. Stone, H. Jun, X. Wang, M. Bathe, Programming structured DNA assemblies to probe biophysical processes. *Annu. Rev. Biophys.* **48**, 395–419 (2019).
9. A. J. Lee, C. Wälti, DNA nanostructures: A versatile lab-bench for interrogating biological reactions. *Comput. Struct. Biotechnol. J.* **17**, 832–842 (2019).
10. S. Nummelin, B. Shen, P. Piskunen, Q. Liu, M. A. Kostiainen, V. Linko, Robotic DNA nanostructures. *ACS Synth. Biol.* **9**, 1923–1940 (2020).
11. M. M. C. Bastings, F. M. Anastassacos, N. Ponnuswamy, F. G. Leifer, G. Cuneo, C. Lin, D. E. Ingber, J. H. Ryu, W. M. Shih, Modulation of the cellular uptake of DNA origami through control over mass and shape. *Nano Lett.* **18**, 3557–3564 (2018).
12. C. M. Green, D. Mathur, I. L. Medintz, Understanding the fate of DNA nanostructures inside the cell. *J. Mater. Chem. B* **8**, 6170–6178 (2020).
13. P. Wang, M. A. Rahman, Z. Zhao, K. Weiss, C. Zhang, Z. Chen, S. J. Hurwitz, Z. G. Chen, D. M. Shin, Y. Ke, Visualization of the cellular uptake and trafficking of DNA origami sanostructures in cancer cells. *J. Am. Chem. Soc.* **140**, 2478–2484 (2018).
14. E. Lin-Shiao, W. G. Pfeifer, B. R. Shy, M. Saffari Doost, E. Chen, V. S. Vykunta, J. R. Hamilton, E. C. Stahl, D. M. Lopez, C. R. Sandoval Espinoza, A. E. Deyanov, R. J. Lew, M. G. Poirer, A. Marson, C. E. Castro, J. A. Doudna, CRISPR–Cas9-mediated nuclear transport and genomic integration of nanostructured genes in human primary cells. *Nucleic Acids Res.* **50**, 1256–1268 (2022).
15. J. A. Kretzmann, A. Liedl, A. Monferrer, V. Mykhailiuk, S. Beerkens, H. Dietz, Gene-encoding DNA origami for mammalian cell expression. *Nat. Commun.* **14**, 1017 (2023).
16. X. Wu, C. Yang, H. Wang, X. Lu, Y. Shang, Q. Liu, J. Fan, J. Liu, B. Ding, Genetically encoded DNA origami for gene therapy in vivo. *J. Am. Chem. Soc.* **145**, 9343–9353 (2023).
17. T. Misteli, Protein dynamics: Implications for nuclear architecture and gene expression. *Science* **291**, 843–847 (2001).
18. D. L. Spector, A. I. Lamond, Nuclear speckles. *Cold Spring Harb. Perspect. Biol.* **3**, a000646 (2011).
19. J. Hahn, L. Y. T. Chou, R. S. Sørensen, R. M. Guerra, W. M. Shih, Extrusion of RNA from a DNA-origami-based nanofactory. *ACS Nano* **14**, 1550–1559 (2020).
20. H. Ijäs, I. Hakaste, B. Shen, M. A. Kostiainen, V. Linko, Reconfigurable DNA origami nanocapsule for pH-controlled encapsulation and display of cargo. *ACS Nano* **13**, 5959–5967 (2019).
21. A. Sprengel, P. Lill, P. Stegemann, K. Bravo-Rodriguez, E.-C. Schöneweiß, M. Merdanovic, D. Gudnason, M. Aznauryan, L. Gamrad, S. Barcikowski, E. Sanchez-Garcia, V. Birkedal, C. Gatsogiannis, M. Ehrmann, B. Saccà, Tailored protein encapsulation into a DNA host using geometrically organized supramolecular interactions. *Nat. Commun.* **8**, 14472 (2017).
22. F. C. Zanacchi, C. Manzo, A. S. Alvarez, N. D. Derr, M. F. Garcia-Parajo, M. Lakadamyali, A DNA origami platform for quantifying protein copy number in super-resolution. *Nat. Methods* **14**, 789–792 (2017).
23. E. Silvester, B. Vollmer, V. Pražák, D. Vasishtan, E. A. Machala, C. Whittle, S. Black, J. Bath, A. J. Turberfield, K. Grünewald, L. A. Baker, DNA origami signposts for identifying proteins on cell membranes by electron cryotomography. *Cell* **184**, 1110–1121.e16 (2021).
24. G. Grossi, M. D. E. Jepsen, J. Kjems, E. S. Andersen, Control of enzyme reactions by a reconfigurable DNA nanovault. *Nat. Commun.* **8**, 992 (2017).
25. G. Grossi, A. Jaekel, E. S. Andersen, B. Saccà, Enzyme-functionalized DNA nanostructures as tools for organizing and controlling enzymatic reactions. *MRS Bull.* **42**, 920–924 (2017).
26. T. Funck, F. Nicoli, A. Kuzyk, T. Liedl, Sensing picomolar concentrations of RNA using switchable plasmonic chirality. *Angew. Chem. Int. Ed. Engl.* **57**, 13495–13498 (2018).
27. I. Domljanovic, M. Loretan, S. Kempter, G. P. Acuna, S. Kocabey, C. Ruegg, DNA origami book biosensor for multiplex detection of cancer-associated nucleic acids. *Nanoscale* **14**, 15432–15441 (2022).
28. J. V. Le, Y. Luo, M. A. Darcy, C. R. Lucas, M. F. Goodwin, M. G. Poirier, C. E. Castro, Probing nucleosome stability with a DNA origami nanocaliper. *ACS Nano* **10**, 7073–7084 (2016).
29. J. J. Funke, P. Ketterer, C. Lieleg, S. Schunter, P. Korber, H. Dietz, Uncovering the forces between nucleosomes using DNA origami. *Sci. Adv.* **2**, e1600974 (2016).
30. Q. Pan, C. Nie, Y. Hu, J. Yi, C. Liu, J. Zhang, M. He, M. He, T. Chen, X. Chu, Aptamer-functionalized DNA origami for targeted codelivery of antisense oligonucleotides and doxorubicin to enhance therapy in drug-resistant cancer cells. *ACS Appl. Mater. Interfaces* **12**, 400–409 (2020).
31. M. M. C. Bastings, Cellular uptake of DNA origami, in *DNA and RNA Origami*, J. Valero, Ed. (Springer, 2023); https://link.springer.com/10.1007/978-1-0716-3028-0_13, vol. 2639 of *Methods in Molecular Biology*, pp. 209–229.
32. A. Liedl, J. Grießing, J. A. Kretzmann, H. Dietz, Active nuclear import of mammalian cell-expressible DNA origami. *J. Am. Chem. Soc.* **145**, 4946–4950 (2023).
33. S. Conic, D. Desplancq, A. Ferrand, V. Fischer, V. Heyer, B. R. S. Martin, J. Pontabry, M. Oulad-Abdelghani, K. B. N, G. D. Wright, N. Molina, E. Weiss, L. Tora, Imaging of native transcription factors and histone phosphorylation at high resolution in live cells. *J. Cell Biol.* **217**, 1537–1552 (2018).
34. S. Conic, D. Desplancq, L. Tora, E. Weiss, Electroporation of labeled antibodies to visualize endogenous proteins and posttranslational modifications in living Metazoan cell types. *Bio Protocol* **8**, e3069 (2018).
35. S. Conic, D. Desplancq, A. Ferrand, N. Molina, E. Weiss, L. Tora, Visualization of endogenous transcription factors in single cells using an antibody electroporation-based imaging approach, in *Imaging Gene Expression*, Y. Shav-Tal, Ed. (Springer, 2019); http://link.springer.com/10.1007/978-1-4939-9674-2_14, vol. 2038 of *Methods in Molecular Biology*, pp. 209–221.
36. P. D. Halley, C. R. Lucas, E. M. M. Williams, M. J. Webber, R. A. Patton, C. Kural, D. M. Lucas, J. C. Byrd, C. E. Castro, Daunorubicin-loaded DNA origami nanostructures circumvent drug-resistance mechanisms in a leukemia model. *Small* **12**, 308–320 (2016).
37. C. R. Lucas, P. D. Halley, A. A. Chowdury, B. K. Harrington, L. Beaver, R. Lapalombella, A. J. Johnson, E. K. Hertlein, M. A. Phelps, J. C. Byrd, C. E. Castro, DNA origami nanostructures elicit dose-dependent immunogenicity and are nontoxic up to high doses in vivo. *Small* **18**, e2108063 (2022).
38. S. M. Douglas, A. H. Marblestone, S. Teerapittayanon, A. Vazquez, G. M. Church, W. M. Shih, Rapid prototyping of 3D DNA-origami shapes with caDNAno. *Nucleic Acids Res.* **37**, 5001–5006 (2009).
39. P. D. Halley, R. A. Patton, A. Chowdhury, J. C. Byrd, C. E. Castro, Low-cost, simple, and scalable self-assembly of DNA origami nanostructures. *Nano Res.* **12**, 1207–1215 (2019).
40. B. E. K. Snodin, F. Randisi, M. Mosayebi, P. Šulc, J. S. Schreck, F. Romano, T. E. Ouldridge, R. Tsukanov, E. Nir, A. A. Louis, J. P. K. Doye, Introducing improved structural properties and salt dependence into a coarse-grained model of DNA. *J. Chem. Phys.* **142**, 234901 (2015).
41. E. Poppleton, R. Romero, A. Mallya, L. Rovigatti, P. Šulc, OxDNA.org: A public webserver for coarse-grained simulations of DNA and RNA nanostructures. *Nucleic Acids Res.* **49**, W491–W498 (2021).
42. A. M. Derfus, W. C. W. Chan, S. N. Bhatia, Intracellular delivery of quantum dots for live cell labeling and organelle tracking. *Adv. Mater.* **16**, 961–966 (2004).
43. J. Lin, R. Chen, S. Feng, Y. Li, Z. Huang, S. Xie, Y. Yu, M. Cheng, H. Zeng, Rapid delivery of silver nanoparticles into living cells by electroporation for surface-enhanced Raman spectroscopy. *Biosens. Bioelectron.* **25**, 388–394 (2009).
44. M. Golzio, J. Teissié, M.-P. Rols, Direct visualization at the single-cell level of electrically mediated gene delivery. *Proc. Natl. Acad. Sci. U.S.A.* **99**, 1292–1297 (2002).
45. A. Lacroix, E. Vengut-Climent, D. De Rochambeau, H. F. Sleiman, Uptake and fate of fluorescently labeled DNA nanostructures in cellular environments: A cautionary tale. *ACS Cent. Sci.* **5**, 882–891 (2019).
46. I. Izeddin, V. Récamier, L. Bosanac, I. I. Cissé, L. Boudarene, C. Dugast-Darzacq, F. Proux, O. Bénichou, R. Voituriez, O. Bensaude, M. Dahan, X. Darzacq, Single-molecule tracking in live cells reveals distinct target-search strategies of transcription factors in the nucleus. *eLife* **3**, e02230 (2014).
47. W. Engelen, H. Dietz, Advancing biophysics using DNA origami. *Annu. Rev. Biophys.* **50**, 469–492 (2021).
48. S. Zhang, X. Lou, L. Liu, Y. Yang, The creation of DNA origami-based supramolecular nanostructures for cancer therapy. *Adv. Healthc. Mater.* **12**, e2301066 (2023).
49. M. Raveendran, A. J. Lee, R. Sharma, C. Wälti, P. Actis, Rational design of DNA nanostructures for single molecule biosensing. *Nat. Commun.* **11**, 4384 (2020).
50. Q. Mei, X. Wei, F. Su, Y. Liu, C. Youngbull, R. Johnson, S. Lindsay, H. Yan, D. Meldrum, Stability of DNA origami nanoarrays in cell lysate. *Nano Lett.* **11**, 1477–1482 (2011).
51. S. Goltry, N. Hallstrom, T. Clark, W. Kuang, J. Lee, C. Jorcyk, W. B. Knowlton, B. Yurke, W. L. Hughes, E. Graugnard, DNA topology influences molecular machine lifetime in human serum. *Nanoscale* **7**, 10382–10390 (2015).
52. J. Hahn, S. F. J. Wickham, W. M. Shih, S. D. Perrault, Addressing the instability of DNA nanostructures in tissue culture. *ACS Nano* **8**, 8765–8775 (2014).
53. H. Bila, E. E. Kurisinkal, M. M. C. Bastings, Engineering a stable future for DNA-origami as a biomaterial. *Biomater. Sci.* **7**, 532–541 (2019).
54. N. Ponnuswamy, M. M. C. Bastings, B. Nathwani, J. H. Ryu, L. Y. T. Chou, M. Vinther, W. A. Li, F. M. Anastassacos, D. J. Mooney, W. M. Shih, Oligolysine-based coating protects DNA

nanostructures from low-salt denaturation and nuclease degradation. *Nat. Commun.* **8**, 15654 (2017).
55. T. Gerling, M. Kube, B. Kick, H. Dietz, Sequence-programmable covalent bonding of designed DNA assemblies. *Sci. Adv.* **4**, eaau1157 (2018).
56. Y. Yang, Q. Lu, C. Huang, H. Qian, Y. Zhang, S. Deshpande, G. Arya, Y. Ke, S. Zauscher, Programmable site-specific functionalization of DNA origami with polynucleotide brushes. *Angew. Chem. Int. Ed. Engl.* **60**, 23241–23247 (2021).
57. A. Chopra, S. Krishnan, F. C. Simmel, Electrotransfection of polyamine folded DNA origami structures. *Nano Lett.* **16**, 6683–6690 (2016).
58. D. Mathur, K. E. Rogers, S. A. Díaz, M. E. Muroski, W. P. Klein, O. K. Nag, K. Lee, L. D. Field, J. B. Delehanty, I. L. Medintz, Determining the cytosolic stability of small DNA nanostructures in cellula. *Nano Lett.* **22**, 5037–5045 (2022).
59. A. S. Walsh, H. Yin, C. M. Erben, M. J. A. Wood, A. J. Turberfield, DNA cage delivery to mammalian cells. *ACS Nano* **5**, 5427–5432 (2011).
60. X. Shen, Q. Jiang, J. Wang, L. Dai, G. Zou, Z.-G. Wang, W.-Q. Chen, W. Jiang, B. Ding, Visualization of the intracellular location and stability of DNA origami with a label-free fluorescent probe. *Chem. Commun.* **48**, 11301 (2012).
61. D. Balakrishnan, G. D. Wilkens, J. G. Heddle, Delivering DNA origami to cells. *Nanomedicine* **14**, 911–925 (2019).
62. X. Chen, B. Jia, Z. Lu, L. Liao, H. Yu, Z. Li, Aptamer-integrated scaffolds for biologically functional DNA origami structures. *ACS Appl. Mater. Interfaces* **13**, 39711–39718 (2021).
63. J. A. G. Briggs, T. Wilk, R. Welker, H.-G. Kräusslich, S. D. Fuller, Structural organization of authentic, mature HIV-1 virions and cores. *EMBO J.* **22**, 1707–1715 (2003).
64. D. Forget, A.-A. Lacombe, P. Cloutier, M. Lavallée-Adam, M. Blanchette, B. Coulombe, Nuclear import of RNA polymerase II is coupled with nucleocytoplasmic shuttling of the RNA polymerase II-associated protein 2. *Nucleic Acids Res.* **41**, 6881–6891 (2013).
65. N. Freitas, C. Cunha, Mechanisms and signals for the nuclear import of proteins. *Curr. Genomics* **10**, 550–557 (2009).
66. Y. Ke, S. M. Douglas, M. Liu, J. Sharma, A. Cheng, A. Leung, Y. Liu, W. M. Shih, H. Yan, Multilayer DNA origami packed on a square lattice. *J. Am. Chem. Soc.* **131**, 15903–15908 (2009).
67. T. G. Martin, H. Dietz, Magnesium-free self-assembly of multi-layer DNA objects. *Nat. Commun.* **3**, 1103 (2012).
68. Y. Ke, G. Bellot, N. V. Voigt, E. Fradkov, W. M. Shih, Two design strategies for enhancement of multilayer–DNA-origami folding: Underwinding for specific intercalator rescue and staple-break positioning. *Chem. Sci.* **3**, 2587–2597 (2012).
69. R. Kosinski, A. Mukhortava, W. Pfeifer, A. Candelli, P. Rauch, B. Saccà, Sites of high local frustration in DNA origami. *Nat. Commun.* **10**, 1061 (2019).
70. T. E. Ouldridge, A. A. Louis, J. P. K. Doye, Structural, mechanical, and thermodynamic properties of a coarse-grained DNA model. *J. Chem. Phys.* **134**, 085101 (2011).
71. A. Suma, E. Poppleton, M. Matthies, P. Šulc, F. Romano, A. A. Louis, J. P. K. Doye, C. Micheletti, L. Rovigatti, TacoxDNA: A user-friendly web server for simulations of complex DNA structures, from single strands to origami. *J. Comput. Chem.* **40**, 2586–2595 (2019).
72. E. C. Meng, T. D. Goddard, E. F. Pettersen, G. S. Couch, Z. J. Pearson, J. H. Morris, T. E. Ferrin, UCSF ChimeraX: Tools for structure building and analysis. *Protein Sci.* **32**, e4792 (2023).
73. W. E. M. Noteborn, L. Abendstein, T. H. Sharp, One-pot synthesis of defined-length ssDNA for multiscaffold DNA origami. *Bioconjug. Chem.* **32**, 94–98 (2021).
74. C.-Y. Oh, E. R. Henderson, A Comparison of methods for the production of kilobase-length single-stranded DNA. *DNA* **2**, 56–67 (2022).
75. M. R. Green, J. Sambrook, Precipitation of DNA with ethanol. *Cold Spring Harb Protoc.* **2016**, doi:10.1101/pdb.prot093377 (2016).
76. C. E. Castro, F. Kilchherr, D.-N. Kim, E. L. Shiao, T. Wauer, P. Wortmann, M. Bathe, H. Dietz, A primer to scaffolded DNA origami. *Nat. Methods* **8**, 221–229 (2011).
77. W. G. Pfeifer, C.-M. Huang, M. G. Poirier, G. Arya, C. E. Castro, Versatile computer-aided design of free-form DNA nanostructures and assemblies. *Sci. Adv.* **9**, eadi0697 (2023).
78. A. Kucinic, C.-M. Huang, J. Wang, H.-J. Su, C. E. Castro, DNA origami tubes with reconfigurable cross-sections. *Nanoscale* **15**, 562–572 (2023).
79. E. Stahl, T. G. Martin, F. Praetorius, H. Dietz, Facile and scalable preparation of pure and dense DNA origami solutions. *Angew. Chem. Int. Ed. Engl.* **53**, 12735–12740 (2014).
80. A. E. Marras, L. Zhou, H.-J. Su, C. E. Castro, Programmable motion of DNA origami mechanisms. *Proc. Natl. Acad. Sci. U.S.A.* **112**, 713–718 (2015).
81. J. Schindelin, I. Arganda-Carreras, E. Frise, V. Kaynig, M. Longair, T. Pietzsch, S. Preibisch, C. Rueden, S. Saalfeld, B. Schmid, J.-Y. Tinevez, D. J. White, V. Hartenstein, K. Eliceiri, P. Tomancak, A. Cardona, Fiji: An open-source platform for biological-image analysis. *Nat. Methods* **9**, 676–682 (2012).
82. N. Otsu, A threshold selection method from gray-level histograms. *IEEE Trans. Syst. Man Cybern.* **9**, 62–66 (1979).
83. S. Bolte, F. P. Cordelières, A guided tour into subcellular colocalization analysis in light microscopy. *J. Microsc.* **224**, 213–232 (2006).
84. O. Glushonkov, E. Réal, E. Boutant, Y. Mély, P. Didier, Optimized protocol for combined PALM-dSTORM imaging. *Sci. Rep.* **8**, 8749 (2018).
85. J. Brocher, biovoxxel/BioVoxxel-Toolbox: BioVoxxel Toolbox, version v2.5.3, Zenodo (2022); https://doi.org/10.5281/ZENODO.5986130.

Acknowledgments: We thank the present and past members of the Castro, Poirier, Lakadamyali, Tora, and Arya laboratories for insightful discussions. We thank the University of Pennsylvania, Cell and Developmental Biology Core Microscopy Facility, and A. Stout for help with iSIM imaging. We also acknowledge support from the Campus Microscopy and Imaging Facility (CMIF) at The Ohio State University for TEM imaging. **Funding:** This work was financially supported by the following: National Science Foundation EFRI grant 1933344 (M.G.P., L.T., M.L., G.A., and C.E.C.), French National Research Agency grant ANR-22-CE11-0013-01_ACT (L.T.), Fondation pour la Recherche Médicale EQU-2021-03012631 (L.T.), and National Institutes of Health grant R35GM139564 (M.G.P. and L.T.). As part of the ITI 2021-2028 program of the University of Strasbourg, L.T.'s laboratory was also supported by IdEx Unistra (ANR-10-IDEX-0002) and by SFRI-STRAT'US project (ANR 20-SFRI-0012) and EUR IMCBio (ANR-17-EURE-0023) under the framework of the French Investments for the Future Program. **Author contributions:** G.M.R. led all preparation of functionalized and purified DNA origami and performed gel electrophoresis and electron microscopy imaging. P.C. performed fixed-cell HILO imaging experiments and analysis. A.O. performed antibody purification, electroporation, live-cell HILO microscopy experiments, particle tracking live-cell experiments, and data analysis. E.M.S. performed electroporation and confocal and iSIM imaging. W.P. designed the DNA origami structures, performed simulation of some DNA origami designs, and supported electron microscopy analysis. S.S. supported functionalization and purification of DNA origami structures. Y.W. supported the fabrication, gel electrophoresis, and electron microscopy characterization of DNA origami. P.D. supported live-cell HILO microscopy and provided instrumentation for live-cell imaging. M.D. performed simulation of some DNA origami designs and performed particle tracking analyses of live-cell experiments in collaboration with A.O. G.A. supervised the simulation and particle tracking analysis. L.T. together with C.E.C. and M.G.P. developed the original idea of DO conjugation with Pol II antibodies for nuclear delivery. L.T. supervised the antibody preparation, live-cell imaging experiments, and many aspects of the cellular work, and provided funding and facilities. M.L. supervised all fixed-cell imaging experiments, provided general guidance for imaging work, and provided funding and facilities. M.G.P. supervised functionalization and purification of DNA origami, cosupervised characterization of DNA origami, and provided funding and facilities. C.E.C. supervised the DNA origami design and fabrication, cosupervised DNA origami characterization, provided funding and facilities, and led the overall collaborative project. G.M.R., P.C., A.O., and C.E.C. led the drafting of the manuscript with extensive input and feedback from L.T., M.L., M.G.P., and G.A. **Competing interests:** The authors declare that they have no competing interests. **Data and materials availability:** All data needed to evaluate the conclusions in the paper are present in the paper and/or the Supplementary Materials. Codes used are available as described in Materials and Methods. DNA nanostructure designs are available at nanobase.org (https://nanobase.org/structure/237).

Submitted 10 January 2024
Accepted 3 June 2024
Published 5 July 2024
10.1126/sciadv.adn9423